Regular Article

PHYSICAL CHEMISTRY RESEARCH
Published by the
Iranian Chemical Society
www.physchemres.org
info@physchemres.org

Phys. Chem. Res., Vol. 11, No. 3, 575-587, September 2023
DOI: 10.22036/pcr.2022.341626.2099

Synthesis of ZnS Nanoparticles *via* a Sonochemical Method: Photocatalytic Activity and Optical Properties

M. Riazian[a,*] and A. Yekrangisendi[b]

[a]*Department of Engineering, Faculty of Science, Islamic Azad University, Tonekabon Branch, Tonekabon, Iran*
[b]*Department of Engineering, Faculty of Science, Islamic Azad University, Ramsar Branch, Ramsar, Iran*
(Received 10 May 2022, Accepted 1 September 2022)

This paper reports on the synthesis and characterization of zinc sulfide (ZnS) dandelion-like nanoparticles (NPs) *via* a simple and template-free sonochemical method. The elimination of an organic methylene blue (MB) dye, as an organic pollutant, from an aqueous solution was carried out *via* the photodegradation process by ZnS NPs as a photocatalyst under ultraviolet (UV) irradiation. The ZnS NPs were investigated by X-ray diffraction (XRD), field emission scanning electron microscopy (FE-SEM), transmission electron microscopy (TEM), Fourier transform infrared spectroscopy (FT-IR), diffuse reflectance spectroscopy (DRS), energy dispersive X-ray spectroscopy (EDS), ultraviolet-visible (UV-Vis) spectroscopy, and N_2 physical adsorption analysis. The DRS result revealed that the optical band gap energy of ZnS NPs was 3.55 eV. The FE-SEM and TEM showed that the average size of dandelion-like NPs was 60 nm. Furthermore, the Brunauer-Emmett-Teller and Barrett-Joyner-Halenda methods were used to determine the porosity properties, including pore volume, special surface area, and mean pore diameter with the values of 57.72 $\frac{m^3}{g}$, 9.76 $\frac{m^2}{g}$, and 16.5 nm, respectively.

Keywords: Photocatalytic activity, ZnS, Sonochemical, Optical band gap energy

INTRODUCTION

Recently, zinc sulfide (ZnS) has received special attention due to its non-toxic and photocatalytic activity, novel optical properties as well as being economical and environmentally friendly [1-5]. ZnS has been widely utilized in pharmaceutical compounds, semiconductor applications, environmental fields, sensing and imaging, solar window layers, and infrared windows [6-10]. ZnS is a semiconductor that shows two distinct crystalline phases, including cubic (zinc blende) and hexagonal (wurtzite) structures with an optical band gap energy of 3.7-4.8 eV [1-2,5]. The physical and chemical properties of ZnS NPs, such as their optical and photocatalytic activity, strongly depend on the precursor chemistry and three geometric specifications, namely, morphology, dimension, and size. Many researchers are interested in synthesizing and discovering the novel properties of nanoscale materials due to their high effective surface area and high chemical reactivity.

Different morphologies of ZnS NPs, such as hallow [11], nanowires [12], nanorods [13], nanotubes [14], nanoflowers [15], nanosheets [16], and nanoclusters [17] have been fabricated. Various methods, such as hydrothermal [18], solvothermal [19], co-precipitation [20], electro-spray pyrolysis [21], capping agent assisted [22], solid-liquid reaction [23], combustion synthesis [24], laser ablation [25], vapor deposition [26], and sonochemical [27], have been utilized to synthesize the above-mentioned ZnS NPs structures. The synthesis through a sonochemical method is simple, less toxic, low-cost, controllable, and productive [28].

Nowadays, environmental pollution has become an essential challenge [29]. A wide range of complex organic compounds such as pigments, dyes, insecticides, and

*Corresponding author. E-mail: m.riazian@toniau.ac.ir

aromatic compounds pose a serious hazard to the environment since they can enter the surface and source water and eventually the bodies of living organisms [30]. Among the compounds mentioned above, dyes and pigments are considered more dangerous due to their high solubility and high potential for entering the body parts of living organisms. Finally, these compounds may enter the food chain and cause genetic mutations in humans [31]. Conventional wastewater treatment processes, including physical, chemical, and biological methods such as electrolysis, osmotic filtration, biodegradation, active carbon adsorption, and ozonation [32], have been applied, yet the outcome of each of these processes depend on efficiency, durability, feasibility, and economic considerations [33]. Advanced oxidation process (AOP), a novel procedure based on semiconductor nanophotocatalysts under UV irradiation, has great efficiency for water splitting, hydrogen and hydroxyl radical production, and pollution elimination from water [34]. The ascendency of AOP over conventional methods in wastewater is due to its strong oxidation power, high photostability, rapid photodegradation rate, high efficiency, and compatibility with subjected organic/inorganic pollutants [2]. Among the semiconductor nanophotocatalysts, nontoxic ZnS NPs have excellent photocatalytic activity due to their novel optical properties, which could vary according to their structure and particle size, proper optical band gap energy, high retention time, the high negative reduction-oxidation potential of excited electrons, and high capacity for the production of electron-hole pairs under UV irradiation in aqueous solutions [35-37]. The general photodegradation mechanism involves the generation of electron-hole ($e^-\_h^+$) pairs after absorbing the sufficient energy of UV-Vis photons (at least equal to the optical band gap) by semiconductors as well as sulfides and transition metal oxides [38-41]. The photogenerated electrons in photocatalysts could transfer from the valance band to the conduction band during UV-Vis irradiation and generate holes, which, in turn, create more free superoxide and hydroxyl radicals on the surface of photocatalysts in contact with water in an aqueous solution. The above-mentioned oxidants (superoxide and hydroxyl radicals) can act as high reactive radicals and attack complex organic pollutants, pesticides, and heavy metallic compounds and degrade them to smaller, simple and harmless fragments and eventually to carbon dioxide and water molecules [2,31,42]. The major challenge to the use of photocatalysis is the slow reaction kinetic rate attributed to the slow generation and fast recombination of the generated ($e^-\_h^+$) pairs. To overcome this obstacle, it has been suggested that semiconductors be modified to photocatalyst NPs, different precursors and suitable supporting additives be utilized, reactive solvents be used, and some metallic or nonmetallic materials be doped [43-45].

In this research, ZnS NPs were characterized and fabricated by a sonochemical method. Furthermore, the optical band gap energy was measured, and the photocatalytic activity of ZnS NPs was determined under UV-Vis irradiation by the photodegradation of conventional, overused, and organic cationic methylene blue (MB) dye. The results were different from those of similar studies [1,2,46].

EXPERIMENTAL PROCEDURES

To fabricate ZnS NPs by a sonochemical method, carbon disulfide (CS_2, ≥ 99%), thiosemicarbazide ($NH_2CSNHNH_2$, ≥ 98%), ethylenediamine ($C_2H_8N_2$, ≥ 99%), zinc chloride ($ZnCl_2$, ≥ 99%), and deionized water were purchased from Merck co. and utilized as precursors without further impurity. Firstly, 0.2 ml of carbon disulfide was dissolved in 40 ml deionized water, and the solution was intensely stirred by a magnet stirrer (5000 rpm) for 15 min. Then, 0.6 ml of ethylenediamine, as a reactive solvent, was drop-wisely added to the stirred solution. The resulting solution was stirred at 5000 rpm for 1 h and sonicated for 15 min at 35 °C (model: Sono Swiss, 100 kHz, 800 W). Thereafter, 0.21 g of zinc chloride was added to 10 ml of deionized water, and the mix was added to the above-mentioned solution. The resulting solution was stirred for 1 h and sonicated for 45 min at 35 °C. The obtained solution was centrifuged at 8000 rpm for 15 min to collect the NPs. The humid precipitate was rinsed several times with deionized water and ethanol to remove impurities. The obtained powder was kept at 60 °C in a furnace and dried for 24 h. Finally, the powder was ground in an agate mortar.

The crystalline characterization of ZnS NPs was analyzed by XRD (model: GBC-MMA) with CuKα radiation

(λ = 0.15418 nm) equipped with a Nickel filter. The intensity of the XRD patterns of ZnS NPs was recorded in the angular range of $20^o \leq 2\theta \leq 55^o$ and determined at room temperature in the step-scan mode with a step rate of 2 deg min^{-1} and a step size of $2\theta = 0.02^o$. Philips CM120 TEM and Hitachi S-4160 FE-SEM equipped with the EDS were utilized to investigate the morphology and compositional analysis of ZnS NPs, respectively. The photocatalytic activity and photodegradation rate of ZnS NPs were evaluated by the degradation of MB dye under UV irradiation (Lamp: Philips, UV-C, 253.70 nm, 40 W) using a UV-Vis spectrophotometer (Varian 50 Scan). Perkin Elmer Prys FT-IR with KBr pellets in the range of 500-4000 cm^{-1} was used to confirm the formed chemical bonds. Shimadzu UV-2550-8030 UV-Vis spectrophotometer with a slit width of 0.5 nm and light source wavelength of 360 nm was applied at room temperature to record the diffuse reflectance spectroscopy (DRS) and the optical absorption of NPs in the range of 200-800 nm.

The photocatalytic degradation of MB was regarded as a measure of the photocatalytic activity of ZnS NPs in an aqueous solution under UV irradiation. The photoreactor consisted of 2 UV-C lamps (Philips, 253.7 nm, 33.6 $\mu W\ cm^{-2}$, 40 W) that were positioned 8 cm above the quartz reservoir. The temperature of the photoreactor was fixed at 27 ± 1 °C by a small ventilator. A stock solution was employed by dispersing 70 mg of ZnS NPs into 100 ml of 3.75 ppm MB solution at pH = 5.5. Before starting the photodegradation experiments, to establish the absorption-desorption equilibrium between the dye and ZnS NPs, all suspensions were kept and sonicated at 40 kHz in a dark place without UV irradiation. The experimental findings did not show a significant effect of visible light on photocatalytic degradation. Afterward, 10 ml of the reaction solution was taken from the stock solution and stored in a quartz vial every 10 min. The adapted reaction solution was illuminated under UV irradiation. The photodegradation reaction continued for 60 min; then, the irradiated solution was centrifuged at 6000 rpm for 5 min and instantly filtered through a 0.1 Millipore membrane to remove the suspended ZnS NPs. Finally, the absorption of the cleaned solution was measured at the maximum absorption of the wavelength (668 nm) by a UV-Vis spectrophotometer (VARIAN, UV-Vis 50 Scan).

RESULTS AND DISCUSSION

The XRD spectrum indicated that the ZnS NPs had partly an amorphous structure with a broad peak. As shown in Fig. 1, the prominent peak at $2\theta = 29.09^o$ can be attributed to the plane (111) of the cubic zinc blende crystalline phase. The d-space and Miller indices were determined by the Bragg formula ($n\lambda = 2d\sin\theta$). The structural data, including d-space, cell constant, and unite cell volume of the cubic crystalline phase, were calculated from the lattice geometry equations, as cited below, and were equal to 0.306 nm, 0.530 nm, and 0.149 nm^3, respectively.

$$\frac{1}{d_{hkl}^2} = \frac{h^2+k^2+l^2}{a^2} \quad (1)$$

$$V = a^3 \quad (2)$$

The average crystallite size of ZnS NPs was estimated using Scherrer's equation from the prominent peaks:

$$L = \frac{k\lambda}{\beta_D cos\theta} \quad (3)$$

$$\beta_D = [(\beta)_m^2 - (\beta)_{ins}^2]^{\frac{1}{2}} \quad (4)$$

where L is the crystallite size in nm, k is a shape factor equal to 0.9 for spherical-shaped particles, λ is the x-ray radiation wavelength (0.15418 nm), β_D is the corrected peak width at the half-maximum intensity in radians, β_m is the measured

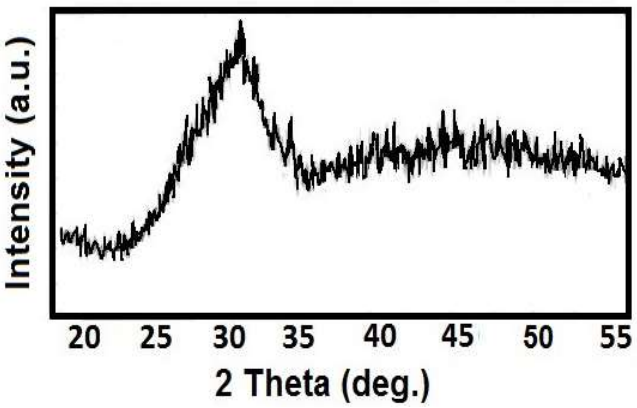

Fig. 1. The XRD patterns of anatase crystalline phase of ZnS NPs.

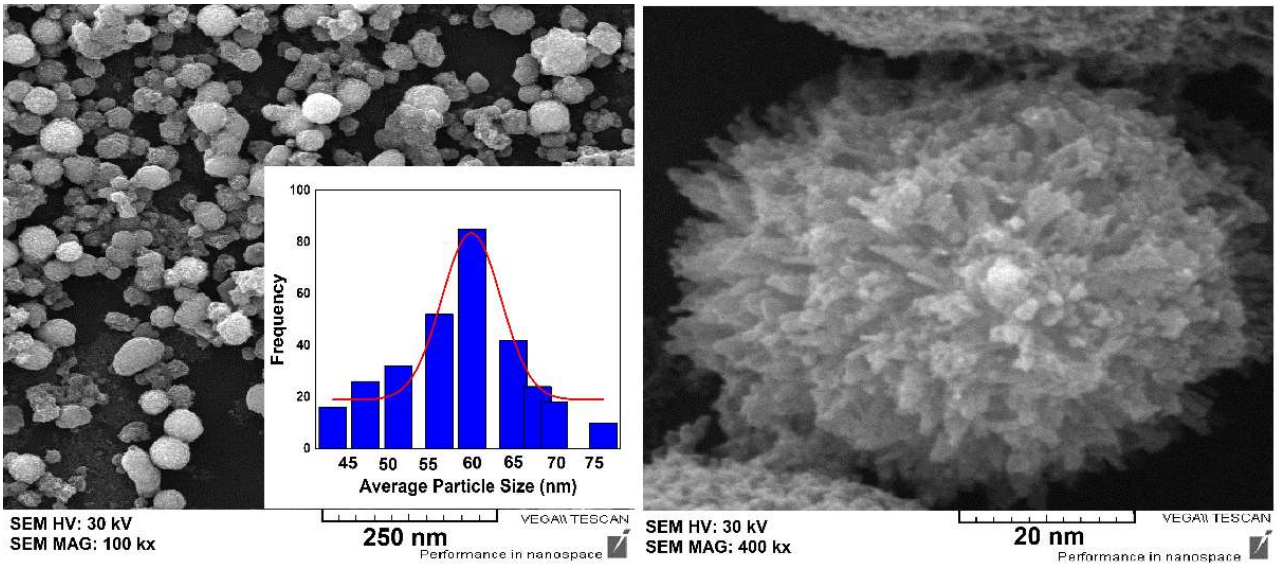

Fig. 2. The SEM images of ZnS NPs at different magnifications.

broadening of the diffraction peak, β_{ins} is the instrumental broadening according to the diffraction patterns of a standard sample such as Si, and θ is the prominent peak position in half diffraction angle (Bragg's angle). Scherrer's equation is a simple and incomplete estimate that considers crystallites to be spherical in shape. According to Scherrer's equation, the average crystallite size was calculated from the sharpest XRD peak (111) to be 28 nm. The X-ray density (ρ) and the specific surface area (Sa) of ZnS nanocrystallites belonging to the sharpest Bragg peak (111) were determined by the following equations [47]:

$$\rho = \frac{\mathrm{n}M}{N_A\, a^3} \tag{5}$$

$$S_a = \frac{6}{L\times\rho} = \frac{S_A}{V\times\rho} \tag{6}$$

where M is the molecular weight, n is the number of atoms associated with each unit tetragonal cell, a and c are lattice constants, L is the ZnS nanocrystallite size, V is the volume of spherical nanocrystallites ($\frac{4}{3}\pi(\frac{D}{2})^3$), N_A stands for the Avogadro's constant, S_A denotes the surface area, and L is the average size of the ZnS nanocrystallite. The S_A, ρ, and $\frac{S_A}{V_{particle}}$ were estimated to be $47.83\frac{m^2}{g}$, $4.34\frac{g}{cm^3}$, and 0.21, respectively.

Figure 2 illustrates the morphology of ZnS NPs. As shown in Fig. 2, the spherical NPs are distributed with an appropriate separation. The size of NPs was determined from the FE-SEM images using a histogram of the distribution of ZnS NPs that was found to be 60 nm. The surface of NPs had a porous and serrated shape. This formation was due to the tendency of NPs to reach lower energy and become more stable particles. Since ZnS NPs were small in size and dendrite in shape, they can behave as a suitable absorber of UV light energy. They also possess an acceptable chemical reactivity to split the complex organic compositions.

Figure 3 shows the energy dispersive of ZnS NPs and confirms the presence of Zn and S atoms. No other peaks representing foreign and irrelevant impurities were observed. As shown in Fig. 3, the highest wt% of S and Zn was found to be 58.22% and 41.78%, respectively. This confirms the presence of ZnS NPs. It is worth noting that the size of ZnS NPs determined from TEM was consistent with the FE-SEM results. As shown in Fig. 4, the average size of ZnS NPs was about 55 nm.

The DRS spectrum of ZnS NPs is shown in Fig. 5a. As shown in Fig. 5, a strong UV absorbance was observed at 300.8 nm. UV-Vis spectrum was utilized to investigate the optical absorption band gap (E_{opt}) of ZnS NPs. E_{opt} can be estimated by the Kubelka-Munk (K-M) and Tauc methods. According to the K-M method (Fig. 5a), E_{opt} is calculated

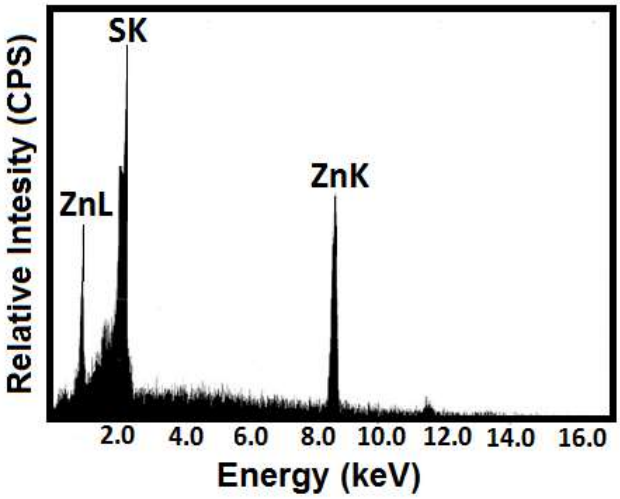

Fig. 3. The EDS spectra of ZnS NPs.

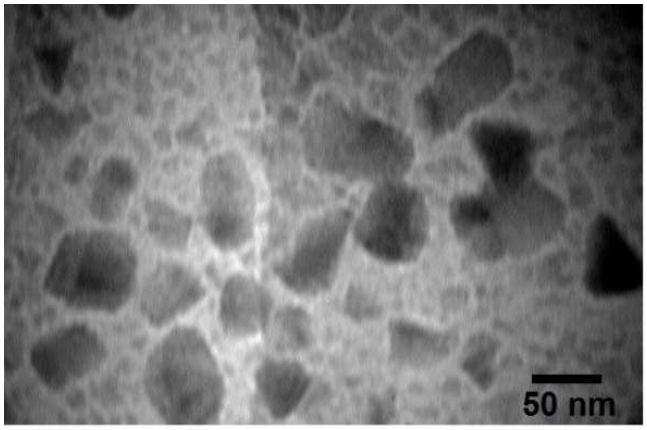

Fig. 4. The TEM image of ZnS NPs.

from the x-axis intercept of the linear extrapolation of the absorption edge. The E_{opt} was estimated to be 3.47 eV using the following equation:

$$\text{Eopt} = \frac{hC}{\lambda} \quad (7)$$

where h, c, and λ stand for Planck's constant (eV), light velocity (m s^{-1}), and linear extrapolated wavelength (360 nm), respectively. The electronic excitation from the valence band to the conduction band was affected by the E_{opt} and absorption edge. Therefore, the results from the K-M had to be verified and confirmed by another method. The E_{opt} of ZnS NPs was determined employing the Tauc equation:

$$\alpha h\upsilon = A(h\upsilon - E_{opt})^n \quad (8)$$

where h is Planck's constant, υ is the incident light frequency, A is the relation constant, and α is the optical absorption coefficient ($\alpha = \frac{2.303\,A}{d}$). The value of power n depends on the type of electronic transmission, *i.e.*, n = 1/2, 2 are for the allowed direct and indirect electronic transition, respectively, while n = 3/2, 3 are for the forbidden direct and indirect transitions, respectively [48-50]. The direct optical band gap of ZnS NPs measured from the Tauc equation was 3.55 eV (Fig. 5b), which is somewhat in agreement with the value calculated from the K-M method. Compared to the commercial bulk ZnS with E_{opt} = 3.68 eV and λ = 350 nm, the E_{opt} of the synthesized ZnS NPs showed a red-shift in the

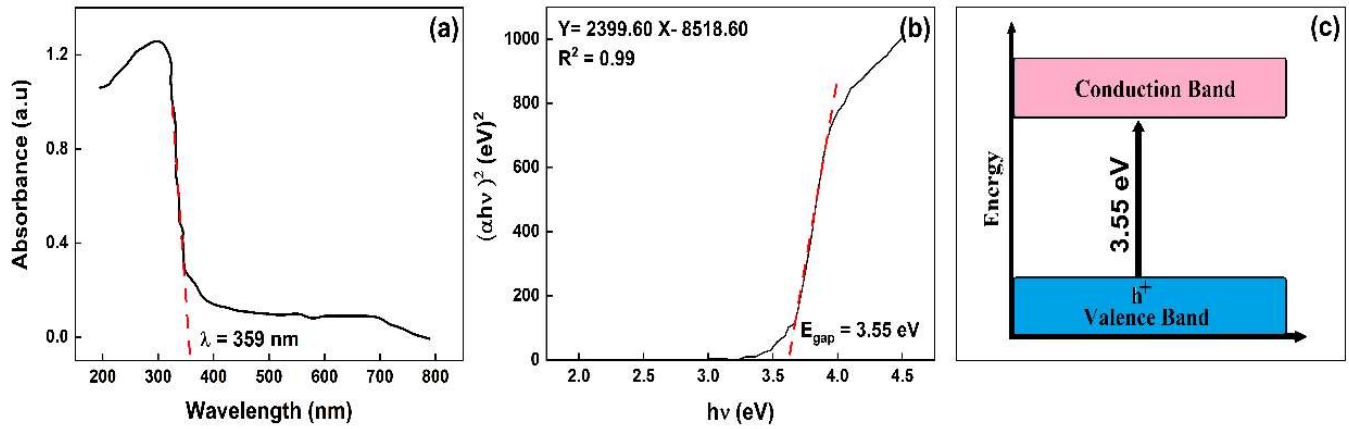

Fig. 5. (a) The DRS (K-M function) of Zn SNPs, (b) the E_{opt} of the Tauc equation from the curve of $(\alpha h\upsilon)^2$ *versus* (hυ), and (c) schematic diagram of energy level within the conduction and valence energy bands.

band gap transition. This shift was due to the size effect that caused extra delocalization of the electronic wave function [2]. This synthesis resulted in the narrowing of the E_{opt} and consequently the extension of the absorption region to the visible light range (Fig. 5c).

The performance of nanophotocatalysts is influenced by two important factors: poor response to the visible light region in the wide optical band gap and low photon efficiency due to its rapid (e^-_h^+) recombination [51-52]. The photocatalytic activity of the fabricated ZnS NPs was evaluated by degrading the MB solution under UV irradiation.

The schematic diagram of the UV-irradiation-driven photodegradation mechanism of ZnS in NPs in an aqueous solution is illustrated in Fig. 6. By absorbing the incident UV photons with the energy equal to or greater than the optical band gap energy of ZnS NPs, the photodegradation reaction began and electron-hole pairs, which were powerful oxidizing and active agents, were generated on the surface of ZnS NPs. The formation of oxidizing and reductive agents (e^--h^+) can be expressed by the following reaction:

$$ZnS + h\upsilon \rightarrow h^+ (VB) + e^- (CB) \quad (8)$$

where VB and CB denote valence and conduction band, respectively. The oxidative and reductive reaction can be expressed as follows:

$$OH^- + h^+ \rightarrow \dot{O}H$$
$$O_2 + 4e^- \rightarrow 2O^{2-} \quad (9)$$

The photogenerated active electrons reduced the surface absorbed oxygen molecules to produce $\cdot O_2^-$ radicals, which decomposed the dyes to harmless and simple molecules [3-4,53]. The excited electrons were trapped by chemisorbed water molecules and/or surface hydroxyl groups to produce $\dot{O}H$ radicals. Also, the dissolved oxygen molecules trapped the excited electrons to produce active superoxide radical ions ($O_2^- \cdot O_2^-$), leading to the production of oxidizing agent hydroperoxy ($HO_2^{\cdot}$) radicals. Ultimately, the active generated radicals attacked and degraded the MB molecules under UV light irradiation, the reaction of which is expressed below [53-54]:

$$MB + HO_2^{\cdot} \rightarrow (CO_2 + H_2O + NH_4^+ + NO_3^+ + SO_4^{-2} + Cl^-) \quad (10)$$

The intensity of the absorption peaks decreased with increasing the irradiation time due to the decoloration of MB dye. Figure 7a reveals the time-dependency of absorption of MB located at 668 nm. The following equation was employed to estimate the photodegradation of MB solution:

$$\text{Degradation percent} = \left[\frac{C_0 - C}{C}\right] \times 100 \quad (11)$$

where Co and C stand for the initial and final dye concentration after UV irradiation time, respectively. Figure 7b illustrates the variation in C_o/C *versus* the irradiation time, and Fig. 7c reveals that the photodegradation percent after 60 min of irradiation was about 85%. The kinetic consideration of ZnS NPs photocatalytic activity was

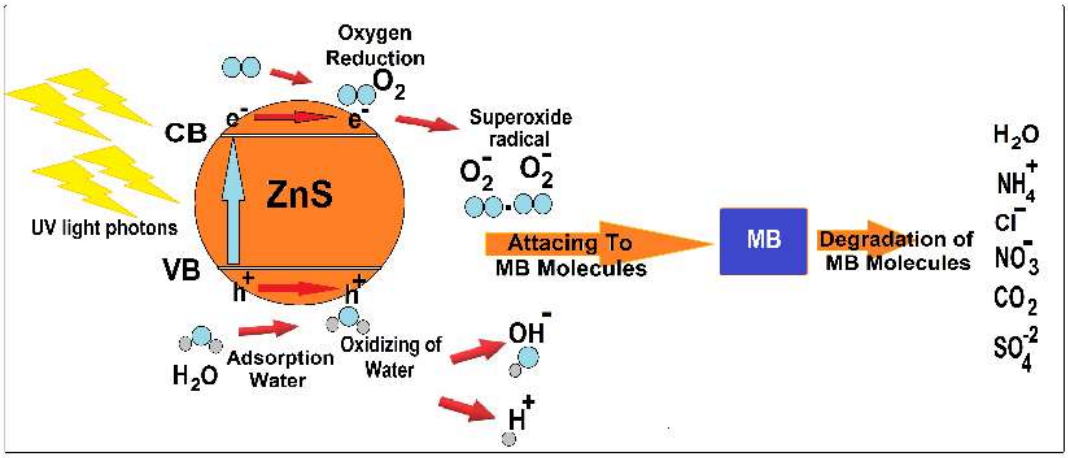

Fig. 6. A feasible mechanism for the photodegradation reaction.

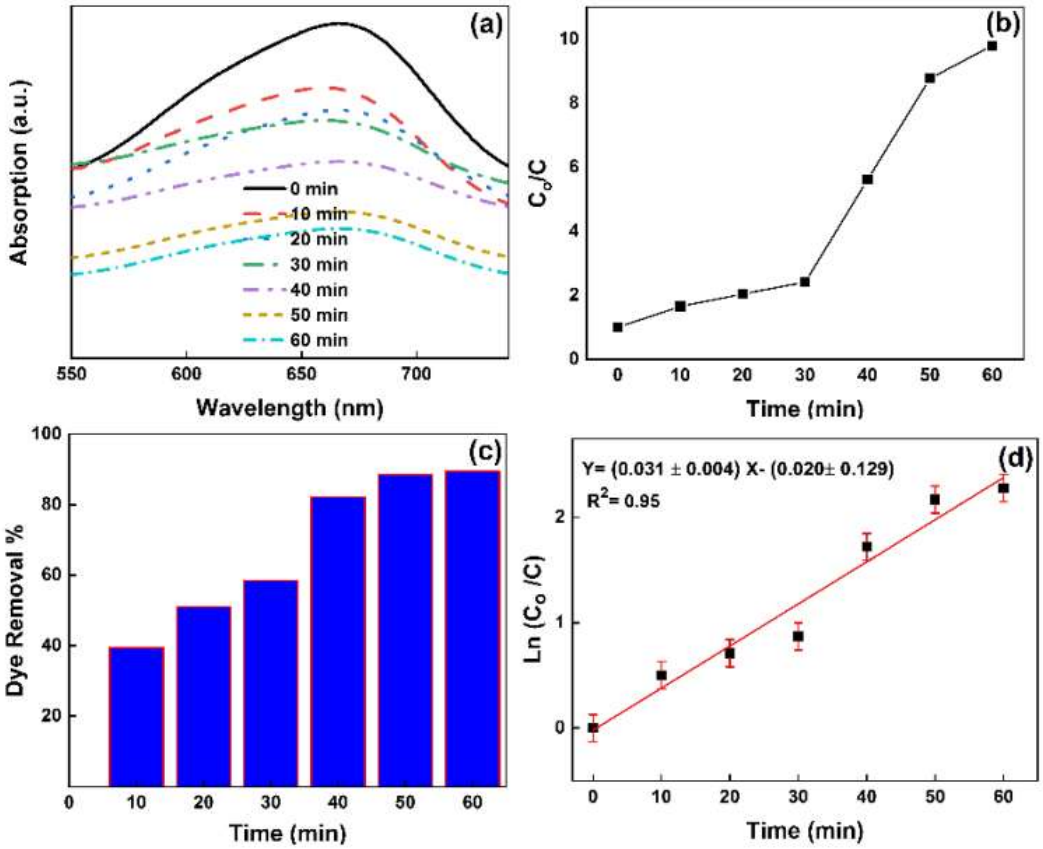

Fig. 7. (a) UV-Vis absorption spectrum of MB aqueous solution in the presence of ZnS NPs, (b) photocatalytic degradation of MB against irradiation time, (c) the dye removal percent *versus* the irradiation time for MB, and (d) the kinetic linear relation between ln(C_o/C) and irradiation time for MB.

carried out by the Langmuir-Hinshelwood model at low MB concentration. According to this model, the kinetic calculation of the photodegradation of ZnS NPs can be simplified to a linear relation by the pseudo-first-order kinetic model. Figure 7d shows the variation in ln(C_o/C) versus UV irradiation time fitted as a linear extrapolation by the following equation [1,3,55-56]:

$$k.t = Ln\left[\frac{C_0}{C}\right] \quad (12)$$

where k stands for the photodegradation rate constant (1/min) and was estimated to be 0.031 1/min.

To specify and confirm the chemical bonds of metallic and ceramic oxides of ZnS NPs, the FT-IR spectrum in the range of 500-4000 cm^{-1} was applied. As shown in Fig. 8, the

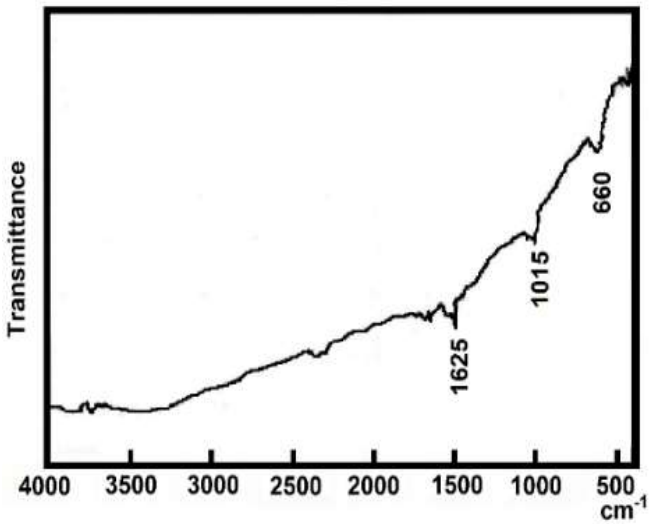

Fig. 8. FT-IR spectra of ZnS NPs.

peaks occurred at 1625, 1015, and 660 cm^{-1}. The peak at 1625 cm^{-1} can be attributed to the bending vibration of hydroxyl groups. Furthermore, the bands present at 657 and 1012 cm^{-1} are related to the Zn-S vibration bond [57]. The absence of any other peak confirms the formation of Zn-S chemical bonding in the NPs as well as the complete progress of the reaction in the sonochemical method.

The obtained adsorption-desorption isotherm plots of ZnS NPs are illustrated in Fig. 9. The surface area analysis and porosity characteristics of the synthesized ZnS NPs were carried out using Brunauer-Emmett-Teller (BET) and Barrett-Joyner-Halenda (BJH) methods. The physical surface area was determined using the BET method by measuring the adsorption against the relative pressure in static equilibrium. The N_2 adsorption-desorption isotherm was accomplished at 77 K over the range of $0.15 < P/P_o < 0.81$. The N_2 physical adsorption isotherm was classified into the IV type. Also, the hysteresis loop was that of H2 according to the International Union of Pure and Applied Chemistry (IUPAC). The IV type of physical adsorption isotherm implied capillary condensation in meso- and macro-pores while closure at about $P/P_o \sim 0.15$ reflected the presence of small mesopores. Figure 9b shows the BET-specific surface area, which was calculated to be 9.76 $m^2\ g^{-1}$. Pore size distribution, total pore volume, the volume of mesopores (V_m), mean pore diameter (r_m), and the peak of the pore size (r_{peak}) in pore size distribution were determined using the BJH method, as presented in Fig. 9c. The physical adsorption profile shows that 86.14% of porosity was located in the mesopores. The porosity parameters of ZnS NPs are summarized in Table 1.

The properties of the synthesized NPs are listed in Table 2 and compared to previous studies with different methods and precursors [1,46], According to Table 2, the photocatalytic activity of ZnS NPs synthesized by a sonochemical method was less than that of other samples. The synthesized NPs also had a larger optical band gap and a smaller specific surface area (S_{BET}), which together explain the reduced photodegradation rate compared to that of other samples. As presented in Table 2, ZnS NPs exhibited two types of crystalline polymorphous, the cubic zinc blende and hexagonal (wurtzite) structures with a direct wide optical band gap in the range of 3.7-4.8 eV caused by the difference

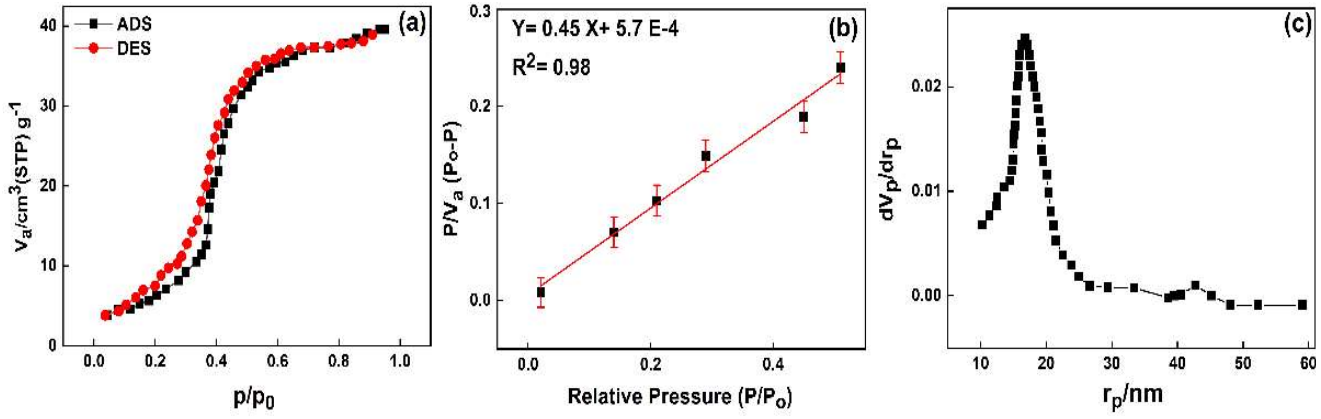

Fig. 9. (a) N_2 adsorption-desorption isotherm, (b) the BET plot, and (c) the BJH plot of ZnS NPs.

Table 1. N_2 Physical Adsorption Data of the Synthesized ZnS NPs

Total pore volume ($\frac{m^3}{g}$)	V_m ($\frac{m^3}{g}$) STP	Specific surface area ($\frac{m^3}{g}$)	Average pore diameter (nm)	$r_{p,peak}$ (nm)
57.72	49.71	9.76	23.65	16.73

Table 2. Summary of Specifications and Photodegradation Properties of Synthesized ZnS NPs

Synthesized method	Precursors	Crystalline phase	Specific surface area ($\frac{m^3}{g}$)	Optical absorption band gap (eV)	The average size of NPs (nm)		Removal efficiency after 60 min (%)	photodegradation rate constant ($\frac{1}{min}$)
					FE-SEM	TEM		
Hydrothermal	Zinc acetate dehydrate, thiosemicarbazide, ethylenediamine	Wurtzite	20.80	3.43	70	60	80	0.035
Hydrothermal	Thioacetamide, oleic acid, zinc chloride	Zinc blende	19.12	3.47	105	110	95	0.052
Sonochemical	Carbon disulfide, ethylenediamine, thiosemicarbazide	Zinc blende	9.76	3.55	60	55	85	0.031

in atomic arrangement and different Zn and S terminated surfaces [1,58-60]. In the hydrothermal method, the photodegradation rate of NPs in the cubic zinc blende crystalline phase was more than that of those NPs in the hexagonal wurtzite samples [59-60]. This change can be attributed to the atomic arrangement in the crystalline structure of the synthesized NPs, which ultimately led to a reduction in the optical band gap and an increase in the photocatalytic activity in the zinc blende crystalline phase. Phase control is a crucial parameter in the modification of electro-optic properties of semiconductor NPs. According to the experimental findings, the optical band gap and specific surface area are the key factors affecting the photocatalytic activity of ZnS NPs because a lower optical band gap absorbs a wider range of incident photon energies near the visible region, which, in turn, can result in more photodegradation activity.

CONCLUSIONS

In summary, the ZnS NPs were successfully synthesized by a sonochemical method, and their structure, optical band gap, and photocatalytic activity were studied. The X-ray diffraction technique indicated partly amorphous context and cubic zinc blende, with the prominent peak at 29.09° corresponding to (111) lattice plane. The size of zinc blende nanocrystallites was estimated to be 28.9 nm using Scherrer's equation. The size and serrated shape of ZnS NPs were determined by the FE-SEM and TEM images. According to the depicted histogram, the average size of the synthesized ZnS NPs was determined to be about 60 nm. The N_2 adsorption-desorption technique was used to determine the physical surface properties, such as porosity, specific surface area, total pore volume, pore size distribution, and the porosity of the ZnS NPs. The K-M method and Tauc equation were used to calculate the optical band gap, which gave 3.47 eV and 3.55 eV, respectively. The photocatalytic activity of ZnS NPs was determined by measuring the photodegradation rate and the efficiency of the organic MB dye. The chemical bonds and vibration modes of ZnS NPs were illustrated by the FT-IR spectrum. The photocatalytic activity of ZnS NPs was affected by three primary factors: crystalline phase, specific surface area, and optical band gap. Compared to the former synthesized samples, the sample synthesized by the hydrothermal method in cubic zinc blende crystalline phase had the highest photocatalytic activity.

ACKNOWLEDGMENTS

The authors acknowledge the financial support of Islamic Azad University, Tonekabon and Ramsar Branches.

REFERENCES

[1] Riazian, M.; Yousefpoor M., Photocatalytic activity, nanostructure and optical properties of 3D ZnS urchin-like via hydrothermal method. *Int. J. Smart. Nano. Mat*. **2020**, *11* (1), 47-64, DOI: org/10.1080/19475411.2019.1710001.

[2] Soleimani, F.; Nezamzadeh-Ejhieh, A., Study of the photocatalytic activity of CdS-ZnS nano-composite in the photodegradation of rifampin in aqueous solution. J. Mat. Res. Tech. **2020**, *9 (6)*, 16237-16251, DOI: org/10.1016/j.jmrt.2020.11.091.

[3] Yu, D.; Fang, H.; Qiu, P.; Meng, F.; Liu. H.; Wang, S.; Lv, P.; Cong, X.; Niu, Q.; Li, T., Improving the Performance of ZnS Photocatalyst in Degrading Organic Pollutants by Constructing Composites with Ag_2O. *Nanomat.* **2021**, *11* (6), 1451-1464, DOI: org/10.3390/nano11061451.

[4] Patel, J.; Singh, A. K.; Carabineiro, S., Assessing the photocatalytic degradation of fluoroquinolone norfloxacin by Mn: ZnS quantum dots: Kinetic study, degradation pathway and influencing factors. *Nanomat*. **2020**, *10* (5), 964-985, DOI: org/10.3390/nano10050964.

[5] Sabaghi, V.; Davar, F.; Fereshteh, Z., ZnS nanoparticles prepared via simple reflux and hydrothermal method: Optical and photocatalytic properties. *Ceramics Int.* **2018**, *44* (7), 7545-56, DOI: org/10.1016/j.ceramint.2018.01.159.

[6] Bardajee, G. R.; Zamani, M.; Sharifi, M.; Mahmoodian, H., Preparation of novel fluorescence nanosensor κC-CdTe/ZnS quantum dots for high accurate detection of Epirubicin. *Mat. Today Comm*. **2021**, *26,* 101874, DOI: org/10.1016/j.mtcomm.2020.101874-85.

[7] Arab, N.; Fotouhi, L.; Salis, A., Electrosynthesised CdS@ZnS quantum dots decorated multi walled carbon nanotubes for analysis of propranolol in biological fluids and pharmaceutical samples. *Microchem. J.* **2021**, *168*, 106453-64, DOI: org/10.1016/j.microc.2021.106453.

[8] Adel, R.; Ebrahim, S.; Shokry, A.; Soliman, M.; Khalil, M., Nanocomposite of CuInS/ZnS and Nitrogen-Doped Graphene Quantum Dots for Cholesterol Sensing. *ACS Omega*. **2021**, *6* (3), 2167-76, DOI: org/10.1021/acsomega.0c05416.

[9] Son, S.; Jeon, S.; Bae, J. H.; Lee, S. Y.; Chae, D.; Chae, J. Y.; Paik, T.; Lee, H.; Oh, S. J., Efficient radiative cooling emitter adopting the wavelength conversion of giant CdSe/ZnS core-shell nanocrystals. *Mat. Today Phys*. **2021**, *21*, 100496-512, DOI: org/10.1016/j.mtphys.2021.100496.

[10] Janani, R.; Melvin, A. A.; Singh, S., Facile one pot in situ synthesis of ZnS-$ZnIn_2S_4$ composite for improved photocatalytic applications. *Mat. Sci. Semicond. Proc.* **2021**, *122*, 105480-96, DOI: org/10.1016/j.mssp.2020.105480.

[11] Hu, Y.; Hu, B.; Yang, D.; Wei, Z., Cooperation effects of Cu and Mn impurities inducing the formation of hollow shell structured ZnS quantum dots. *Mat. Tech*. **2021**, *13*, 1-10, DOI: org/10.1080/10667857.2021.1938357.

[12] Ren, H.; Ye, K.; Chen, H.; Zhou, X.; Wang, F.; Shi, Q.; Diao, G.; Chen, M., Polytyped wurtzite-nH ZnS (n = 2, 8): Facile synthesis and photocatalytic hydrogen production under sacrificial reagents. *New J. Chem*. **2021**, *45* (29), 13119-26, DOI: org/10.1039/D1NJ02432A.

[13] Maiti, S.; Manna, G.; Karmakar, S.; Maji, S.; Mukhopadhyay, M. K.; Acharya. S.; Sanyal, M. K., Ordering of ZnS Nanorods at the Air-Liquid Interface: An *In Situ* X-ray Scattering Study. *J. Phys. Chem. C.* **2021**, *125* (23), 12774-83, DOI: org/10.1021/acs.jpcc.1c02277.

[14] Chen, S.; Li, G.; Yang, M.; Xiong, J.; Akter, S.; Mi. L.; Li, Y., Nanotube assembled coral-like ZnS@N,S co-doped carbon: A sodium-ion batteries anode material with outstanding stability and rate performance. *Appl. Surf. Sci.* **2021**, *535*, 147748-56, DOI: org/10.1016/j.apsusc.2020.147748.

[15] Xi, Y.; Hu, C.; Feng, B.; Wang, X.; Zheng, C.; He, X., Synthesis of ZnS nanoflowers by composite-hydroxide-mediated approach. *J. Supercond. Novel Magn.* **2010**, *23* (6), 901-3, DOI: org/10.1007/s10948-009-0642-y.

[16] Feng, W.; Yuan, J.; Zhang, L.; Hu, W.; Wu, Z.; Wang, X.; Huang, X.; Liu, P.; Zhang, S., Atomically thin ZnS nanosheets: Facile synthesis and superior piezocatalytic H_2 production from pure H_2O. *App, Catal. B: Envir.* **2020**, *277*, 119250,

DOI: org/10.1016/j.apcatb.2020.119250.

[17] Liu, S., Yu, Q.; Zhang, C.; Zhang, M.; Rowell, N.; Fan, H.; Huang, W.; Yu, K.; Liang, B., Transforma;ion of ZnS precursor compounds to magic-size clusters exhibiting optical absorption peaking at 269 nm. *J. Phy. Chem. lett.* **2019**, *11* (1), 75-82, DOI: org/10.1021/acs.jpclett.9b02999.

[18] Xin, M.; Liao, L. M.; Han, F., Optical properties of ZnS: Ce nanocrystals prepared by hydrothermal method. *J. Luminescence*. **2021**, *238*, 18074-84, DOI: org/10.1016/j.jlumin.2021.118074.

[19] Zhang, Y. C.; Wang, G. Y.; Hu, X. Y.; Chen, W. W., Solvothermal synthesis of uniform hexagonal-phase ZnS nanorods using a single-source molecular precursor. *Mat. Res. Bull*. **2006**, *41* (10), 1817-24, DOI: org/10.1016/j.materresbull.2006.03.016.

[20] Krsmanović W. R.; Montone, A.; Pietrelli, L.; Pilloni, L., On Tailoring Co-Precipitation Synthesis to Maximize Production Yield of Nanocrystalline Wurtzite ZnS. *Nanomat*. **2021**, *11* (3), 715-26, DOI: org/10.3390/nano11030715.

[21] Doe, T.; Ishikawa, Y.; Horita, M.; Nishida, T.; Uraoka, Y., Size Control of ZnS Nanoparticles by Electro-Spray Deposition Method. *Jpn. J. App. Phys*. **2012**, *51* (3S), 03CC02, DOI: 10.7567/JJAP.51.03CC02.

[22] Samanta, D.; Chanu, T. I.; Chatterjee, S., Citrus limetta juice as capping agent in hydrothermal synthesis of ZnS nanosphere for photocatalytic activity. *Mat. Res. Bull*. **2017**, *88*, 85-90, DOI: org/10.1016/j.materresbull.2016.11.019.

[23] She, Y. Y.; Juan, Y. A.; Qiu, K. Q., Synthesis of ZnS nanoparticles by solid-liquid chemical reaction with ZnO and Na2S under ultrasonic. *Trans. Nonferrous Metals Soc. China*. **2010**, *20*, s211-5, DOI: org/10.1016/S1003-6326(10)60041-6.

[24] Zahiri, M.; Afarani, M. S.; Arabi, A. M., Combustion synthesis of ZnO/ZnS nanocomposite phosphors. *J. fluorescence*. **2019**, *29* (5), 1227-39, DOI: org/10.1007/s10895-019-02434-9.

[25] Wang, D.; Zhang, H.; Li, L.; Chen, M.; Liu, X., Laser-ablation-induced synthesis of porous ZnS/Zn nano-cages and their visible-light-driven photocatalytic reduction of aqueous Cr(VI). *Opt. Mat. Exp.* **2016**, *6* (4), 1306-12, DOI: org/10.1364/OME.6.001306.

[26] Benamra, H.; Saidi, H.; Attaf, A.; Aida, M. S.; Derbali, A.; Attaf, N., Physical properties of Al-doped ZnS thin films prepared by ultrasonic spray technique. *Surf. Interfaces*. **2020**, *21*, 100645-56, DOI: org/10.1016/j.surfin.2020.100645.

[27] Bakhtkhosh, P.; Mehrizad, A., Sonochemical synthesis of Sm-doped ZnS nanoparticles for photocatalytic degradation of Direct Blue 14: experimental design by response surface methodology and development of a kinetics model. *J. Molecular Liquids*. **2017**, *240*, 65-73, DOI: org/10.1016/j.molliq.2017.05.053.

[28] Alkahtani, S. A.; Mahmoud, A. M.; Mahnashi, M. H.; AlQarni, A. O.; Alqahtani, Y. S.; El-Wekil, M. M., Facile one pot sonochemical synthesis of layered nanostructure of ZnS NPs/rGO nanosheets for simultaneous analysis of daclatasvir and hydroxychloroquine. *Microchem. J*. **2021**, *164*, 105972-85, DOI: org/10.1016/j.microc.2021.105972.

[29] Lima, V. B.; Goulart, L. A.; Rocha, R. S.; Steter, J. R.; Lanza, M. R., Degradation of antibiotic ciprofloxacin by different AOP systems using electrochemically generated hydrogen peroxide. *Chemosphere*. **2020**, *247*, 125807-19, DOI: org/10.1016/j.chemosphere.2019.125807.

[30] Gopinath, K. P.; Madhav, N. V.; Krishnan, A.; Malolan, R.; Rangarajan, G., Present applications of titanium dioxide for the photocatalytic removal of pollutants from water: A review. *J. Env. Manag*. **2020**, *270*, 110906, DOI: org/10.1016/j.jenvman.2020.110906.

[31] Sethy, N. K.; Arif, Z.; Mishra, P. K.; Kumar, P., Green synthesis of TiO_2 nanoparticles from Syzygium cumini extract for photo-catalytic removal of lead (Pb) in explosive industrial wastewater. *Green Proc. Syn*. **2020**, *9* (1), 171-81, DOI: org/10.1515/gps-2020-0018.

[32] Zwiener, C. F.; Frimmel, F. H., Oxidative treatment of pharmaceuticals in water. *Water Res*. **2000**, *34* (6), 1881-5, DOI: org/10.1016/S0043-1354(99)00338-3.

[33] Sin, J. C.; Lam, S. M.; Mohamed, A. R.; Lee K. T., Degrading Endocrine Disrupting Chemicals fromWastewater by TiO_2 Photocatalysis: A Review. *Int. J. Photoenergy.* **2012**, *185159*, 1-23, DOI: org/10.1155/2012/185159.

[34] Wang, X.; Chen, N.; Liu, X.; Shi, Y.; Ling, C.; Zhang, L., Ascorbate guided conversion of hydrogen peroxide

to hydroxyl radical on goethite. *Appl. Catal. B: Envir*. **2021**, *282*, 119558 DOI: org/10.1016/j.apcatb.2020.119558.

[35] Zein, R.; Alghoraibi, I., Influence of bath temperature and deposition time on topographical and optical properties of nanoparticles ZnS thin films synthesized by a chemical bath deposition method. *J. Nanomat.* **2019**, *4*, 2019-26, DOI: org/10.1155/2019/7541863.

[36] Yin, L.; Zhang, D.; Wang, D.; Kong, X.; Huang, J.; Wang, F.; Wu, Y., Size dependent photocatalytic activity of ZnS nanostructures prepared by a facile precipitation method. *Mat. Sci. Eng.: B*. **2016**, *208*, 15-21, DOI: org/10.1016/j.mseb.2016.02.004.

[37] Dutková, E.; Daneu, N.; Lukáčová Bujňáková Z.; Baláž, M.; Kováč, J.; Baláž, P., Mechanochemical synthesis and characterization of $CuInS_2$/ZnS nanocrystals. *Molecules*. **2019**, *24* (6), 1031-47, DOI: org/10.3390/molecules24061031.

[38] Balakrishnan, M.; John, R., Properties of sol-gel synthesized multiphase TiO2 (AB)-ZnO (ZW) semiconductor nanostructure: An effective catalyst for methylene blue dye degradation. *Iranian J. Catal*. **2020**, *10* (1), 1-6.

[39] Bhat, S. A.; Zafar, F.; Mondal, A. H.; Kareem, A.; Mirza, A. U.; Khan, S.; Mohammad, A.; Haq, Q. M.; Nishat, N., Photocatalytic degradation of carcinogenic Congo red dye in aqueous solution, antioxidant activity and bactericidal effect of NiO nanoparticles. *J. Iranian Chem. Soc.* **2020**, *17* (1), 215-27, DOI: org/10.1007/s13738-019-01767-3.

[40] Buthiyappan, A.; Aziz, A. R.; Daud, W. M., Recent advances and prospects of catalytic advanced oxidation process in treating textile effluents. Rev. Chem. Eng. **2016**, *32* (1), 1-47, DOI: org/10.1515/revce-2015-0034.

[41] Sadovnikov, S. I., Synthesis, properties and applications of semiconductor nanostructured zinc sulfide. *Russan Chem. Rev.* **2019**, *88* (6), 571-593, DOI: org/10.1070/RCR4867.

[42] Rostami-Vartooni, A.; Moradi-Saadatmand, A.; Bagherzadeh, M.; Mahdavi, M., Green synthesis of $Ag/Fe_3O_4/ZrO_2$ nanocomposite using aqueous Centaurea cyanus flower extract and its catalytic application for reduction of organic pollutants. *Iranian J. Catal.* **2019**, *9* (1), 27-35.

[43] Zhong;, S.; Li, C.; Shen, M.; Lv, C.; Zhang, S., Synthesis of modified bismuth tungstate and the photocatalytic properties on tetracycline degradation and pathways. *J. Mat. Res. Tech*. **2019**, *8* (2), 1849-58, DOI: org/10.1016/j.jmrt.2019.01.002.

[44] Malik, A.; Nath, M., Multicore shell nanocomposite formed by encapsulation of WO_3 in zeolitic imidazolate framework (ZIF-8): as an efficient photocatalyst. *J. Envir. Chem. Eng*. **2019**, *7* (5), 103401, DOI: org/10.1016/j.jece.2019.103401.

[45] Derikvandi, H.; Vosough, M.; Nezamzadeh-Ejhieh, A., A comprehensive study on the enhanced photocatlytic activity of a double-shell mesoporous plasmonic Cu@ Cu_2O/SiO_2 as a visible-light driven nanophotocatalyst. *Envir. Sci. Pollu. Res*. **2020**, *27*, 27582-97, DOI: org/10.1007/s11356-020-08817-x.

[46] Riazian, M.; Yousefpoor, M., Photo-degradation of methylene orange by zinc-sulfide nanoparticles synthesized by hydrothermal method, *Iranian J. Health Envir*. **2021**, *14*, *1*-18.

[47] Mote, V. D.; Purushotham, Y.; Dole, B. N., Structural, morphological and optical properties of Mn doped ZnS nanocrystals. *Cerâmica*. **2013**, *59*, 614-9, DOI: org/10.1590/S0366-69132013000300008.

[48] Abbaspour, S.; Nourbakhsh, A.; Ebrahimi, R.; Ghayour, H.; Mackenzie, K. J., The effect of nanoparticle and mesoporous TiO_2 additions on the electronic characteristics of reduced graphene oxide nanocomposites with zinc oxide under UV irradiation. *Mat. Sci. Eng.: B*, **2019**, *246*, 89-95, DOI: org/10.1016/j.mseb.2019.06.003.

[49] Dianat, S., Visible light induced photocatalytic degradation of direct red 23 and direct brown 166 by $InVO_4$-TiO_2 nanocomposite. *Iranian J. Catal.* **2018**, *8* (2), 121-32.

[50] Pouretedal, H. R.; Fallahgar, M.; Sotoudeh Pourhasan, F.; Nasiri, M., Taguchi optimization of photodegradation of yellow water of trinitrotoluene production catalyzed by nanoparticles TiO_2/N under visible light. *Iranian J. Catal*. **2017**, *7* (4), 317-26.

[51] Chellammal, S.; Sankar, S., Energy gap studies of ZnS nanocrystallites. *Mat. Sci. semicond.Proc*. **2010**, *13* (3), 214-6, DOI: org/10.1016/j.mssp.2010.10.003.

[52] Raksha, K. R.; Ananda, S.; Madegowda, N. M., Study

of kinetics of photocatalysis, bacterial inactivation and •OH scavenging activity of electrochemically synthesized Se^{4+} doped ZnS nanoparticles. *J. Mole. Catal A: Chem.* **2015**, *396*, 319-27, DOI: org/10.1016/j.molcata.2014.10.005.

[53] Emrooz, H. M.; Jalaly, M., Synthesis mechanism of sono-chemically prepared mesoporous ZnS nanoparticles. Mat. Res. Exp. **2017**, *4* (3*)*, 035014-25, DOI: 10.1088/2053-1591/aa61d5.

[54] Houshmand, R.; Banna, M. E. H., Photocatalytic outcomes for methylene blue degradation from CTAB mediated mesoporous ZnS, synthesized with an insoluble precursor in ethanol media. *Nanochem. Res*. **2019**, *4* (1), 64-76, DOI: 10.22036/NCR.2019.01.008.

[55] Zolfaghari, A.; Riazian, M.; Ashjari, M., Photodegradation of Methylene Blue and Evans Blue by Iron and Sulphur Doped TiO_2 Nanophotocatalyst under Ultraviolet and Visible Light Irradiation. *J. Mex. Chem. Soc*. **2021**, *65* (3), 357-375, DOI: org/10.29356/jmcs.v65i3.1516.

[56] Zolfaghari, A.; Riazian, M.; Ashjari, M., Preparation and photodeposition of Fe-S/TiO_2@PEG nanoparticles for methylene blue and Evans blue. *Res. Chem. Intermediates*. **2021**, *47* (5), 1809-28, DOI: org/10.1007/s11164-021-04396-9.

[57] Rojas-Hernandez, A. G.; Mendoza-Pena, K. J.; Troyo-Vega, E.; Perez-Hernandez, C. G.; Munguia-Rodriguez, S.; Mendıvılreynoso, T.; Ramirez-Rodriguez, L. P.; Ochoa-Landin, R.; Alvarez-Ramos, M. E.; Deleon, A.; Castillo, S. J., ZnS nanoparticles synthesized through chemical aggregation using polyethyleneimine that works as both a stabilizer and a complexing agent. *Chalcogenide Lett.* **2017**, *14* (1), 25-30.

[58] Chen, Z. G.; Zou, J.; Liu, G.; Yao, X.; Li, F.; Yuan, X. L.; Sekiguchi, T.; Lu, G. Q.; Cheng, H. M., Growth, cathodoluminescence and field emission of ZnS tetrapod tree-like heterostructures. *Adv. Func. Mat*. **2008**, *18* (19), 3063-9, DOI: org/10.1002/adfm.200800447.

[59] Dai, L.; Lesyuk, R.; Karpulevich, A.; Torche, A.; Bester, G.; Klinke, C., From Wurtzite nanoplatelets to zinc blende nanorods: simultaneous control of shape and phase in Ultrathin ZnS nanocrystals. *J. Phy. Chem Lett*. **2019**, *10* (14), 3828-35, DOI: org/10.1021/acs.jpclett.9b01466.

[60] Yin, L.; Zhang, D.; Ma, J.; Kong, X.; Huang, J.; Zhang, H.; Liu, C., Facile synthesis and characterization of ZnS nano/microcrystallites with enhanced photocatalytic activity. *Powder Tech*. **2016**, *301*, 1085-91, DOI: org/10.1016/j.powtec.2016.07.058.